Energy & Environmental Science

ROYAL SOCIETY OF CHEMISTRY

PAPER

View Article Online
View Journal | View Issue

Cite this: *Energy Environ. Sci.*, 2025, **18**, 3160

Dual-plating aqueous Zn–iodine batteries enabled *via* halogen-complexation chemistry for large-scale energy storage†

Hong Li, ‡[ac] Bosi Huang,‡[a] Mingyan Chuai,‡[de] Zhiyang Zheng,[a] Hao Chen,[b] Zhihong Piao,[a] Guangmin Zhou *[a] and Hong Jin Fan *[bc]

Received 2nd January 2025,
Accepted 12th February 2025

DOI: 10.1039/d5ee00027k

rsc.li/ees

Aqueous Zn–I_2 batteries are promising candidates for grid-scale energy storage due to their low cost, high voltage output and high safety. However, Ah-level Zn–I_2 batteries have been rarely realized due to formidable issues including polyiodide shuttling and zinc dendrites. Here, we develop 10 Ah dual-plating Zn–I_2 batteries (DPZIB) by employing ZnI_xG4(tetraglyme) complex chemistry, in which zinc and iodine are iteratively dissolved and deposited in the aqueous electrolyte. The battery contains no membrane or high-cost electrolytes. The G4 strengthens the Zn–I bond by acting as an electron donor, and meanwhile, it enhances the reductivity of electrolyte by its complexation with Zn^{2+}. Such halogen-complexation chemistry endows static DPZIB with shuttle-free properties, negligible self-discharge, and minimal zinc dendrites. The battery delivers a capacity of 301.5 mA h over 1800 h at 5 mA cm^{-2}, a low capacity decay (0.028% drop per cycle for 800 cycles at 25 mA cm^{-2}), and a scalable capacity of up to 10.8 A h. As a proof of concept, we demonstrate an integrated system encompassing a membrane-free Zn–I_2 flow battery to store solar electricity in the daytime and power electronics at night.

Broader context

Aqueous Zn–I_2 batteries are promising for large-scale energy storage because of the high theoretical capacity and superior safety. However, the short cycle life has been the bottleneck that is caused by both Zn anode instability and polyiodide shuttling. Instead of depositing surface protection layers, it is more technologically viable to engineer the aqueous electrolytes by introducing additives to fundamentally resolve the dissolution of polyiodide from the cathodes and enhance the reversibility of the Zn anode. In this work, we demonstrate a facile dual-plating strategy to construct aqueous Zn–I_2 batteries that can run longer and realize Ah-level capacity. In this design, the active materials of zinc and iodine are iteratively dissolved and deposited, eliminating the requirement of any membrane or electrode framework for either the cathode or anode. Specifically, we utilize ZnI_xG4 complexes, in which three additives (ZnI_2, KI, and G4) work together to inherently diminish the polyiodide ions and prevent the growth of Zn dendrites, leading to enhanced conversion efficiency on both sides. The prototype of flow batteries integrated with photovoltaic panels is demonstrated.

Introduction

Large-scale electrical energy storage (EES) devices are crucial in the extensive deployment of renewable energy, to buffer the impact of intermittent supplies of solar and wind electricity. For this purpose, batteries with the properties of low-cost, high-safety, long-lifespan, and high energy density are required.[1–5] Many rechargeable batteries, such as lithium-ion batteries, zinc–air batteries, lead acid batteries and flow batteries, have been applied for EES systems.[2,6] However, none of them fulfills the above requirements and further improvement remains critically necessary. The focus of energy storage development has shifted from solely maximizing energy density to optimizing the levelized cost of energy, which accounts for energy density, initial cost, and cycling life over the system's lifespan.[7]

[a] *Tsinghua Shenzhen International Graduate School, Tsinghua University, Shenzhen 518055, China. E-mail: guangminzhou@sz.tsinghua.edu.cn*
[b] *School of Physical and Mathematical Sciences, Nanyang Technological University, Singapore 637371, Singapore. E-mail: fanhj@ntu.edu.sg*
[c] *Energy Research Institute@NTU (ERI@N), Nanyang Technological University, Singapore 637553, Singapore*
[d] *State Key Laboratory of Structural Chemistry, Fujian Institute of Research on the Structure of Matter, Chinese Academy of Sciences, Fuzhou 350002, Fujian, China*
[e] *Mindu Innovation Laboratory, Fujian Science & Technology Innovation Laboratory for Optoelectronic Information of China, Fuzhou 350108, Fujian, China*

† Electronic supplementary information (ESI) available. See DOI: https://doi.org/10.1039/d5ee00027k

‡ These authors contributed equally to this work.

In this context, battery systems that leverage non-flammable and cost-efficient aqueous electrolytes present a promising avenue to meet the demands of gigawatt-scale energy storage applications.[8–10] Aqueous Zn–I_2 batteries have emerged as promising candidates for this purpose.[11–15] However, a significant challenge lies in the dissolution of polyiodide species (such as I_3^-/I_5^-), which leads to the loss of active materials and rapid capacity decay. Additionally, the direct interaction between the zinc anode and these shuttling polyiodide intermediates exacerbates zinc corrosion, resulting in diminished coulombic efficiency (CE) and eventually battery failure.[11,13,14,16] This issue becomes even more pronounced in large-scale systems, where the issues of polyiodide shuttling and zinc degradation are more severe.[17–19] To address these challenges, it is crucial to prevent polyiodide shuttling and zinc corrosion for improving the long-term cyclability and scalability of Zn–I_2 batteries.

One prevailing strategy is to employ porous materials as the I_2 host to trap the polyiodide, such as micro-mesoporous carbon, graphene, metal organic frameworks, and covalent organic frameworks.[20–22] However, due to the weak adsorption with polyiodide species, these host materials cannot effectively block the shuttle effect, especially for high-capacity and long-term cycling. Additionally, catalysts were deployed to facilitate the conversion of iodine species to suppress the generation of polyiodide intermediates.[23,24] However, catalysts cannot fundamentally prevent the dissolution of polyiodide from the cathodes. Moreover, the discharge capacities of these 'host–guest' systems are often constrained by the mass of the redox-inactive host materials. Hence, to realize scalable energy storage with Ah-level capacity, it remains highly desirable to explore alternative energy storage mechanisms that maximize the utilization of active materials while ensuring high reversibility for the Zn–I_2 batteries.

Herein, we propose a dual-plating strategy to construct aqueous Zn–I_2 batteries potentially possible for grid-scale energy storage. The dual-plating Zn–I_2 batteries (DPZIB) have a thermodynamically stable working process, in which the active materials of zinc and iodine are iteratively dissolved and deposited, eliminating the requirement of membrane or electrode frameworks for either the cathode or anode. It intrinsically avoids electrode deterioration and failure that happen often to intercalation type electrodes. This dual-plating architecture does not require complicated and time-consuming manufacturing procedures from conventional metal-ion batteries. Fig. 1(a) and (b) illustrate the key difference in the electrolyte structure. We show that the DPZIB operates through a redox-active ZnI_xG4(tetraglyme) complex, which increases the binding between Zn and I, and reconstructs the Zn^{2+} solvated structure. With such halogen-complexation chemistry in the DPZIB, issues of polyiodide shuttling and zinc dendrites are effectively addressed. The constructed static DPZIB delivers a high capacity of 301.5 mA h at 5 mA cm^{-2} after 1800 h of cycling and shows a low capacity decay rate of 0.028% over 800 cycles. As a demonstration, we also constructed membrane-free Zn–I_2 flow batteries powered by silicon photovoltaics. Owing to their inherent safety, high cycling stability, and simple manufacturing process, the DPZIB presented in this study might be a feasible alternative to Li-ion batteries in large-scale energy storage.

Results and discussion

Design concept of dual-plating aqueous Zn–I_2 batteries

The zinc anode is highly reversible as a plating electrode in aqueous electrolytes. However, for large-scale systems, the issue of zinc dendrites becomes pronounced during repeated Zn^{2+} plating and stripping. While iodine presents itself as a promising candidate for a reversible halogen plating electrode, the key issues associated with the shuttling of polyiodide ions and aggregation of solid I_2 within the electrolyte must be addressed. In a 1 M zinc sulfate electrolyte, Zn^{2+} forms a solvation structure, $Zn(H_2O)_6^{2+}$, due to its strong interaction with water molecules. This solvation structure facilitates electron transfer from the water molecules to the cation *via* the metal–OH bond, which in turn weakens the O–H bond. Consequently, this promotes zinc dendrites and the hydrogen evolution reaction (HER) at the zinc metal anode.

To mitigate these issues, in our design, we introduced ZnI_2 and KI into the zinc sulfate electrolyte, in which halogen ions can partially participate in the solvation structure of $Zn(H_2O)_6^{2+}$ to form $ZnI(H_2O)_5^+$ owing to its robust coordination capability with transition metal ions. But this is still insufficient for achieving highly reversible plating as the additives cannot bind with intermediate product I_3^- nor prevent the formation of free iodine ions. To strengthen the binding between Zn^{2+} and polyiodide ions, we introduce a G4 additive as a strong electron donor into the electrolytes. The lone pair of oxygen atoms in G4 allows it to coordinate with Zn^{2+},[25] and the redistribution of charges may enhance the interaction between Zn and I, thus preventing the generation of free iodine ions, which will be proved in the later section. Notably, the G4 donates electrons to the entire solvation structure and weakens the electron transfer from H_2O to Zn^{2+}, enabling the suppression of HER and Zn anode corrosion. In a nutshell, this approach may address key challenges in aqueous Zn–I_2 batteries by ensuring both the stability of the zinc anode and the efficiency of iodine plating, paving the way for long cycle life and scalable energy storage systems.

Electrolyte structure evolution

Molecular dynamics simulation (MD) was conducted to quantify and elucidate the evolution of the Zn^{2+} solvation structure of three electrolytes: $ZnSO_4$ (Z), $ZnSO_4$ + ZnI_2 + KI (ZI), and $ZnSO_4$ + ZnI_2 + KI + G4 (ZIG). The ZIG electrolytes were prepared by dispersing a certain amount KI and ZnI_2 in 0.7 M $ZnSO_4$ aqueous electrolytes with 0.4 M G4 as an additive (denoted as ZIG(0.4 M)). In the pure $ZnSO_4$ electrolyte, $Zn(H_2O)_6^{2+}$ is confirmed as the dominant solvation structure, with a coordination number (CN) of Zn–O(H_2O) reaching 5.80 and an average coordination distance of ~2.15 Å (Fig. 1(e) and Fig. S1, ESI†). Upon the addition of KI and ZnI_2, the I^- occupies the Zn^{2+} solvation shell to form $ZnI(H_2O)_5^+$ evidenced by a

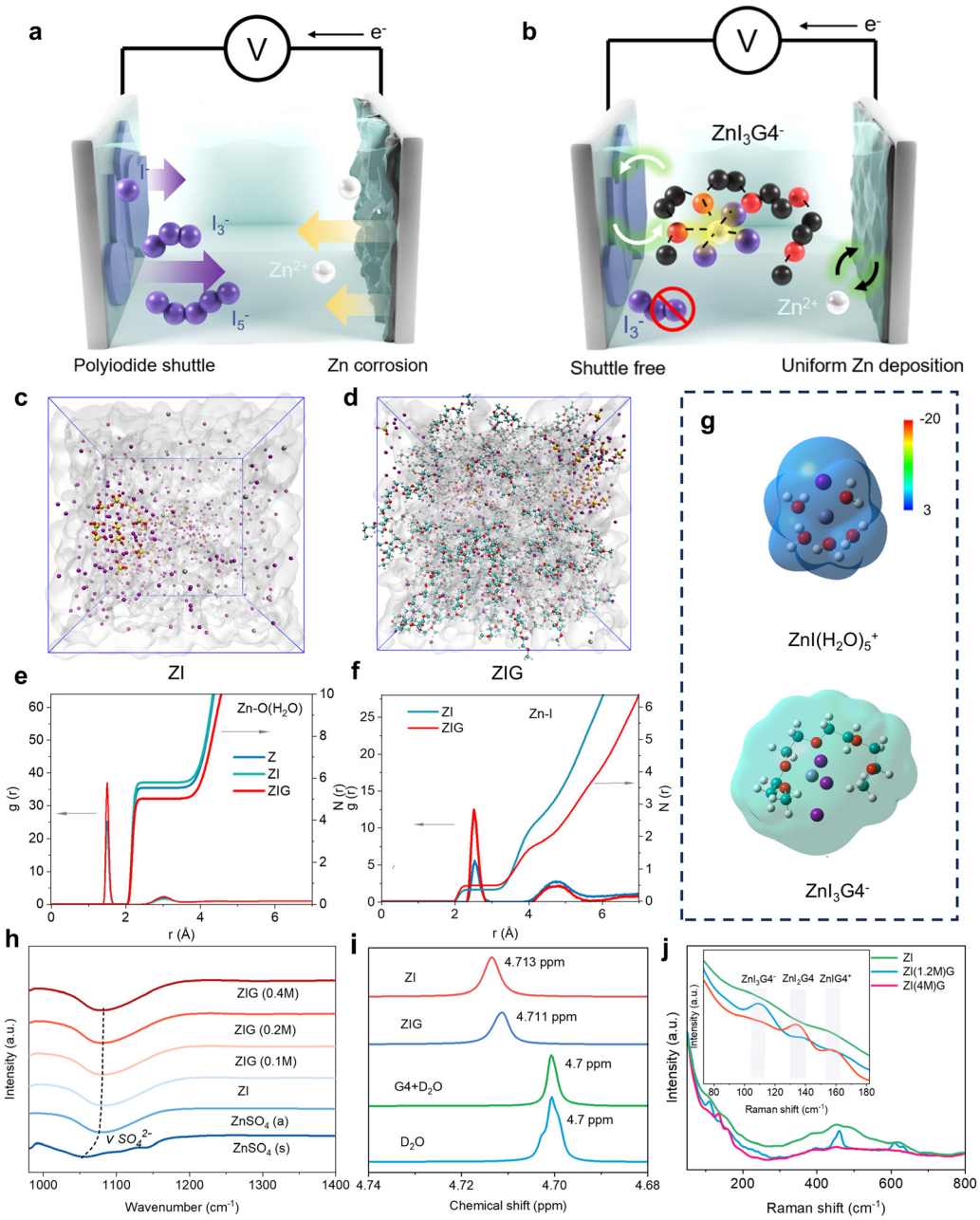

Fig. 1 The concept of DPZIB and the electrolyte structure evolution. (a) Schematic illustration of the traditional Zn–I_2 batteries and (b) our dual-plating Zn–I_2 batteries. The MD snapshots of (c) ZI and (d) ZIG electrolytes. Radial distribution functions and the coordination number for (e) Zn–O (H_2O) and (f) Zn–I. (g) Electrostatic potential distributions of $ZnI(H_2O)_5^+$ (upper) and ZnI_3G4^- (bottom). (h) FTIR spectra for $ZnSO_4$(s), $ZnSO_4$(a) and ZIG with different amounts of G4; (i) ^2H NMR spectra of H_2O in pure D_2O, G4 + D_2O, ZI and ZIG. (j) Raman spectra of ZI and ZIG electrolytes with different concentrations of iodine ion.

sharp Zn–I peak at 2.53 Å and a CN of 0.38, while the CN of Zn–O(H_2O) decreases to 5.5 (Fig. 1(c)–(f)). After G4 was further added, the solution immediately became strikingly yellow (Fig. S2, ESI†), indicating the formation of complex compounds between G4 and the original species in the ZI electrolyte. The added G4 molecules replace the solvated H_2O from the primary Zn^{2+} solvation shell and weaken the CN of Zn–O(H_2O) from 5.5 to 5.0, demonstrating the superior capability of G4 to remove coordinated water (Fig. 1(d) and (f)). This is also confirmed by the Zn–O(G4) coordination structure with a pair peak of 2.1 Å and the CN of 2.9 (Fig. S3, ESI†). Moreover, the CN of the Zn–I coordination structure increases from 0.38 to 0.48 to form ZnI_3G4^- with the addition of G4. Owing to the strong electron-donating ability of the –COC– group in G4 molecules, the electrostatic potential in the solvation structure ZnI_3G4^- is lower compared with $ZnI(H_2O)_5^+$ and $Zn(H_2O)_6^{2+}$ (Fig. 1(g) and Fig. S4, ESI†). The low electrostatic potential can effectively shield the repulsion between Zn^{2+}, providing the ZIG with the highest ionic conductivity (47.6 mS cm^{-2}) to make the Zn^{2+} diffusion more kinetically favored (Fig. S5, ESI†). Therefore,

MD results suggest that G4 partially replaces the original H_2O molecules to adjust the Zn^{2+} solvation structure and diminishes the free iodine ions by constructing $ZnI_3G4(yH_2O)^-$.

More evidence to the solvation structure evolution is provided by spectroscopy results. The Fourier transform infrared (FTIR) spectra presents a negative shift from 1055 to 1076 cm^{-1} after the $ZnSO_4$ powders dissolve in the aqueous solution (Fig. 1(h)). This noticeable blue shift suggests the generation of the primary Zn^{2+} solvation shell with weakened interaction between SO_4^{2-} and Zn^{2+}. The vibration stretching of SO_4^{2-} ($\nu(SO_4^{2-})$) shifts to higher wavenumbers after the addition of ZnI + KI or ZnI + KI + G4. As the amount of G4 additive increases to 0.4 M, the $\nu(SO_4^{2-})$ gradually increases from 1080 to 1082 cm^{-1}, implying a modification in the solvation structure of Zn^{2+} with the addition of G4. These results suggest the G4 molecules participate in the primary Zn^{2+} solvation shell formation and weaken the solvation interaction with H_2O and Zn^{2+}. The influence of the G4 molecules on solvated H_2O molecules was investigated *via* liquid-phase nuclear magnetic resonance (^2H NMR) analyses conducted in various electrolyte solutions utilizing D_2O as the solvent (Fig. 1(i)). In comparison to pure D_2O and D_2O/G4, the ^2H resonance peak in ZI electrolytes exhibits a shift from 4.7 ppm to 4.713 ppm. This shift can be attributed to a decrease in the electron density of neighboring atoms, resulting in a reduced shielding effect on the protons in H_2O molecules. The result suggests the robust coordination between H_2O and Zn^{2+} that decreases the number of free H_2O molecules. However, after the introduction of G4 molecules into ZI electrolytes, the peak moves back to 4.711 ppm, indicating that the G4 molecules participate in the coordination environment of Zn^{2+}, thereby releasing the partially confined H_2O molecules. Raman spectroscopy was performed to analyze the potential solvation structure of Zn^{2+} with different concentrations of I^- (1.2 M I^- and 4 M I^- were denoted as ZI(1.2 M)G and ZI(4 M)G, respectively). New peaks located at 100–160 cm^{-1}, corresponding to the zinc–iodine complexes, are observed only when both I^- and G4 are present (Fig. S6, ESI†). The observed Raman peaks at about 110 cm^{-1} are assigned to ZnI_3G4^- species in the ZI(1.2 M)G4 while peaks appearing at 133, and 159 cm^{-1} are attributed to ZnI_2G4, and $ZnIG4^+$ species in the ZI(4 M)G, respectively. Raman results suggest that once G4 and iodide co-salts (KI + ZnI_2) are added into the $ZnSO_4$ electrolyte, I^- could be detained by the complex superhalide ions (*e.g.*, ZnI_3G4^-), demonstrating the synergistic halogen-complexation process and effective diminishing of free iodide *via* adding G4 and I^- (Fig. 1(j)).[7,16]

Theoretical insights into halogen-complexation chemistry

The halogenation-complex mechanism is further analyzed *via* density functional theory (DFT) calculations. The Gibbs free energy for the formation of ZnI_xG4 (x = 1, 2, 3) superhalides was calculated (Fig. 2(a)). Both G4 and I^- exhibit robust coordination capability with Zn^{2+} to partially replace H_2O with energetically favorable structures (Fig. S7 and S8, ESI†). These formed superhalides ($ZnIG4^+$, ZnI_2G4, and ZnI_3G4^-) are exothermic with negative Gibbs free energy, suggesting that the process is thermodynamically feasible. The maximum coordination of three iodide ions in the ZnI_xG4 superhalides is attributed to two key factors: the steric hindrance from the functional group of G4 and the reduced Lewis acidity of Zn^{2+} upon binding with I^-, which limits further ligand coordination (Fig. S9, ESI†). The electrolyte structure influences battery performances stemming from the intricate balance between free iodide species, hydrated Zn^{2+} and Zn^{2+}-complex ions. DFT calculations were conducted to depict the dominant Raman modes of G4, zinc iodide and potassium iodide species in an aqueous medium. As more iodide ions coordinate in the ZnI_xG4 superhalides, the Raman mode frequency decreases from 167 to 111 cm^{-1} (Fig. 2(b)). This trend is consistent with the experimental results (Fig. 1(j)), further validating the presence of ZnI_xG4 superhalides in the ZIG electrolytes. Differential charge density and atomic charge analyses provide insights into the stability of various solvation configurations. The ZnI_xG4 superhalides display higher charge densities than $ZnI(H_2O)_5^+$, suggesting stronger electronic coupling after the G4 complexation (Fig. 2(c) and Fig. S10, ESI†). Due to the stronger electron-donating capability of the –COC– group of G4 compared with water, O with strong electronegativity can donate electrons to both Zn^{2+} and I^-. And G4 blocks the electron transfer from water to Zn^{2+} and enables higher charges of Zn^{2+} and I^- (Fig. 2(d) and Fig. S11, ESI†). As more iodide ions are coordinated in the Zn^{2+}-complex ions, more charge is transferred. This is verified by the changes of the atomic charges. In addition, the bond lengths of Zn–I in $ZnIG4^+$, ZnI_2G4, and ZnI_3G4^- are all shorter than that in the $ZnI(H_2O)_5^+$, suggesting that Zn–I bonds are strengthened after its complexation. The lowest unoccupied molecular orbital (LUMO) energy levels of the various solvation structures are ultimately investigated to assess their reducibility. The ZnI_xG4 superhalides display a higher LUMO energy level compared with both $ZnI(H_2O)_5^+$ and $Zn(H_2O)_6^{2+}$, implying its high reductive stability to resist the HER (Fig. 2(e)). Hence, the identification of ZnI_xG4 species underscores their crucial role as iodide carriers within the electrolyte systems. They efficiently reduce the number of free iodide ions, and suppress the water-induced parasitic reactions. This effect will benefit the cyclic stability of the I_2-based zinc metal anode during deep cycling (to be discussed below).

Energy storage mechanism of DPZIB

To clarify the storage mechanism of the dual-plating Zn–I_2 batteries, the charge/discharge processes were *in situ* inspected under optical microscopy (Fig. 3(a)). In the beginning, only the carbon fibers of the graphite felt, which served as the substrate for iodine deposition, are visible (Fig. 3(b1) and Fig. S12, ESI†). When a charge current is applied for 210 s, yellow iodine films immediately cover the carbon fiber. As the charge depth increases, more iodine is deposited on the carbon fiber, corresponding to darker color. After charging, the electrode was washed with water, and the active material was extracted for UV-visible analysis, which revealed a broad peak at ~200 cm^{-1} corresponding to iodine (Fig. 3(c)). Upon discharging, the iodine that has grown on the carbon fiber gradually fades away.

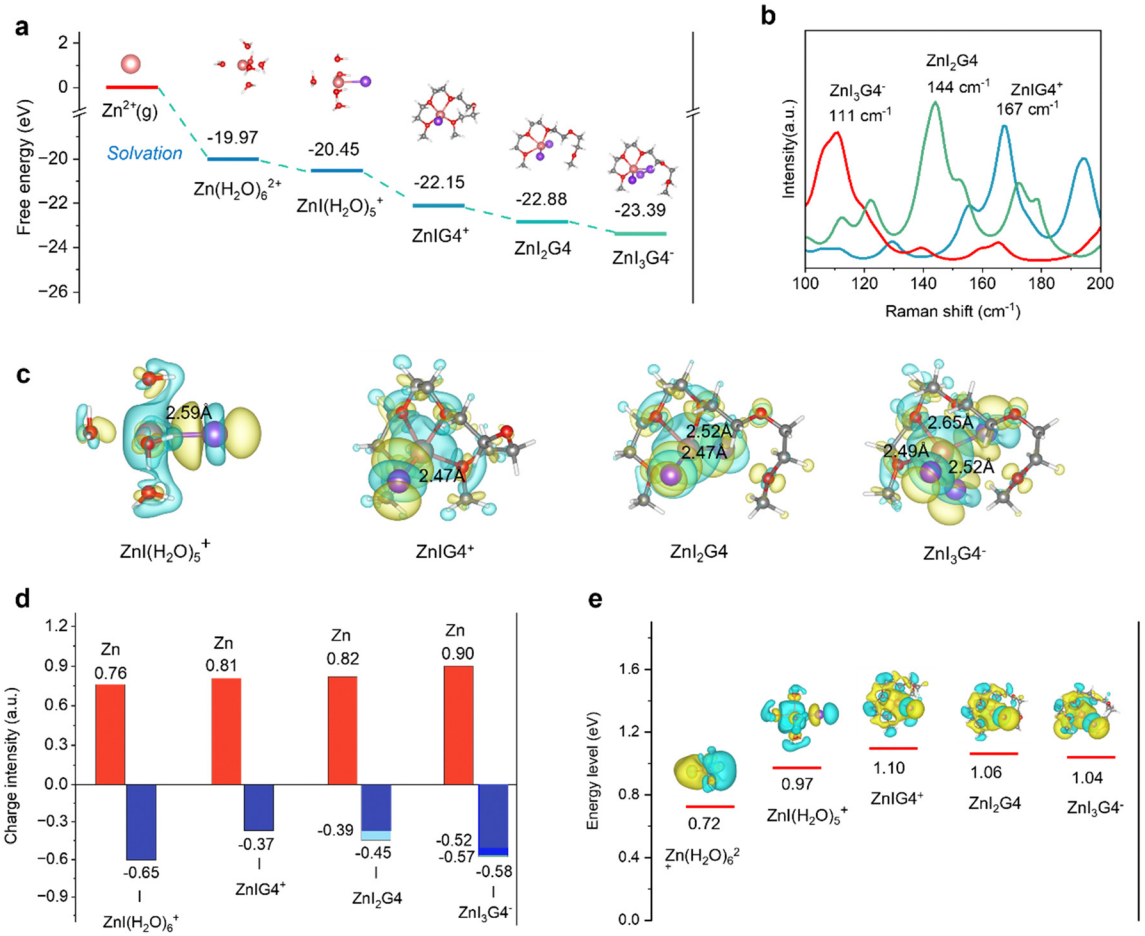

Fig. 2 Theoretical calculations for the electrolyte structures. (a) Free energy change in the Zn^{2+} solvation and halogen-complex transformation processes (C, H, O, Zn, and I atoms are represented by gray, white, red, pink, blue, and violet balls, respectively). (b) DFT calculated major Raman modes of ZnI_2, KI, $ZnSO_4$, and G4 in water. (c) Electron density differences (blue and light-yellow regions denote charge depletion and accumulation, respectively), (d) atomic charge, and (e) LUMO energy of different Zn^{2+} solvation structure.

A few I_2 particles are observed on the carbon fiber at the discharge time of 420 s (Fig. 3(b2)). These observations indicate the reversible I_2 stripping and deposition processes during cycling.

It is commonly agreed that the undesirable polyiodide shuttling is the main problem of the Zn–I_2 batteries. The oxidation of I^- to I_2 during charging produces I_3^- as an intermediate which can easily diffuse to the zinc anode, resulting in serious self-discharging and zinc anode consumption.

$$I_3^- + Zn \rightarrow Zn^{2+} + 3I^- \quad (1)$$

Simultaneously, the regenerated I^- may migrate back to the cathode to react with I_2, accelerating capacity decay and active zinc consumption.

$$I^- + I_2 \rightarrow I_3^- \quad (2)$$

So, to achieve shuttling-free Zn–I_2 batteries, it is essential to prevent the generation of free polyiodide species. In our electrolyte systems, the generation of ZnI_xG4 superhalides effectively diminishes the free iodide ions. Moreover, *in situ* UV-vis experiments demonstrate the appearance of I_3^- during charging and its disappearance after discharging (Fig. 3(d), (e) and Fig. S13, ESI†). These I_3^- intermediates are stabilized in the form of $Zn(I_3)G4^+$ superhalides, as corroborated by *ex situ* Raman spectroscopy and DFT calculations (Fig. 3(f) and Fig. S14, ESI†). The generation of $Zn(I_3)G4^+$ species will greatly restrain Zn anode corrosion by the reduction of free polyiodides. Therefore, the synergistic halogen-complexation chemistry in the electrolytes is expected to mitigate both polyiodide shuttling and zinc dendrite formation. This can be reflected from the self-discharge of the battery, which was assessed by charging it to 1.4 V, allowing it to rest for 96 hours and then discharging to 0.4 V. The cell maintains a high coulombic efficiency (95.6%) with a small voltage drop of 0.018 V (Fig. 3(g)). In addition, the 3D confocal laser scanning microscope (CLSM) image shows no obvious dendrites on the surface of the zinc anode after 30 charge/discharge cycles, where the maximum height is about 17 μm (Fig. 3(h)). Moreover, X-ray diffraction (XRD) and X-ray photoelectron spectroscopy (XPS) were conducted to reveal the surface chemistry of the Zn anode after cycling. XRD patterns reveal weak signals of $Zn_4SO_4(OH)_6{\cdot}4H_2O$ (PDF#44-0673), indicating suppressed corrosion reactions and

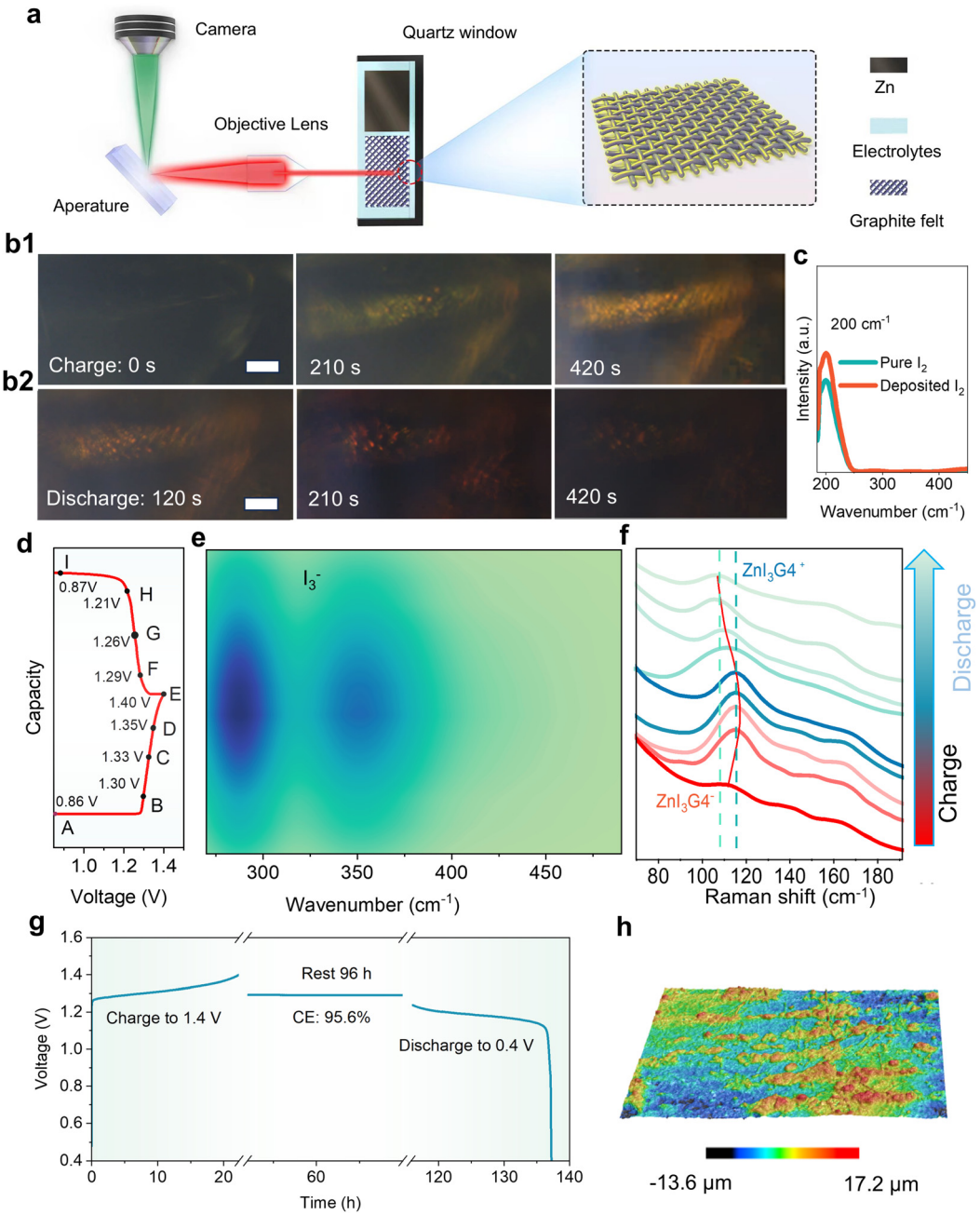

Fig. 3 Energy storage mechanism of the DPZIB. (a) Schematic of the *in situ* microscope experimental setup. (b) Optical microscope images of electrode surface morphology at different charge/discharge time. The scale bars are 10 μm. (c) UV-vis spectra of pure I_2 and the deposited I_2. (d and e) Charge/discharge curves of DPZIB with selective voltages for *in situ* UV-vis tests. (f) The corresponding *ex situ* Raman test. (g) Self-discharge time–potential curves of the DPZIB, and (h) CLSM 3D image of Zn anode after cycling.

minimal by-product formation (Fig. S15, ESI†). And the XPS results suggest that the zinc anode surface is covered by an organic–inorganic layer containing carboxyl organics and I_3^-, which may function as a solid–electrolyte interphase to promote uniform zinc deposition (Fig. S16, ESI†).

Battery performance and potential for scalable energy storage

The aqueous Zn–I_2 dual-plating battery can be assembled by immersing a piece of zinc metal and graphite felt in a homogeneous solution (Fig. 4(a)). The easy structure and low cost of the materials ensures high competency of this battery for scalable implementation. When a normal ZI electrolyte is used, the battery voltage gradually decreases as the charging time increases, even with the increasing current densities (Fig. S17, ESI†). This could be related to polyiodide shuttling and the absence of solid iodine deposition on the carbon felt. For the DPZIB with ZnI_xG4 superhalides, the battery delivers a high initial capacity of 304.1 mA h at the current of 5 mA cm^{-2} with a high energy efficiency of 89.1% (Fig. 4(b)). Here the energy efficiency is defined as the ratio of measured capacity to the

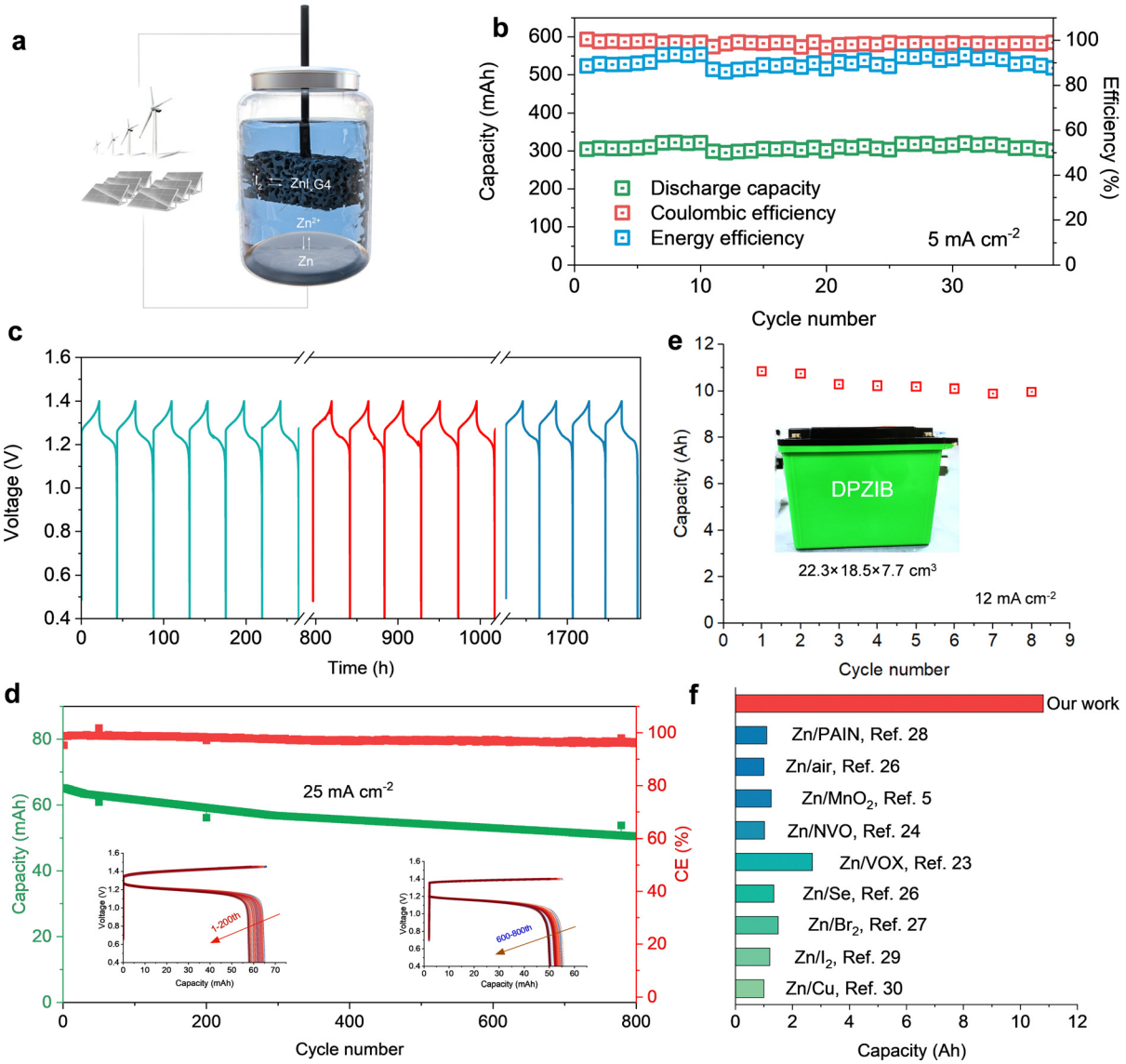

Fig. 4 Electrochemical performance of the DPZIB. (a) Schematic illustration of the configuration of the DPZIB. (b) Cycling performance and (c) time–voltage curves of DPZIB at a current of 5 mA cm^{-2}. (d) Long cycling performance of the DPZIB. (e) Capacity of a large-sized static DPZIB and (f) comparison to various aqueous batteries.

theoretical one. After continuous charge/discharge cycles for over 1800 hours, the battery maintains an average coulombic efficiency of 98.6%, with energy efficiency ranging from 85.9% to 93.7% (Fig. 4(c)). The battery delivers capacities of 313.0, 267.5, 211.2, 163.1, 120.0, and 61.3 mA h at the currents of 5, 10, 15, 18, 20, and 25 mA cm^{-2}, respectively (Fig. S18, ESI†). When the current reduces back to 5 mA cm^{-2}, the capacity recovers back to 310.0 mA h. At a high current of 25 mA cm^{-2}, the battery displays a small capacity decay of 0.028% per cycle with a coulombic efficiency of 97.6% after 800 cycles (Fig. 4(d)). The reversibility is also supported by the highly overlapping of the charge/discharge profiles which consistently exhibit distinct plateaus (inset of Fig. 4(d)). The high reversibility and long-term cycling stability of the static DPZIB are attributed to the iterative dissolution and deposition of cathodes and anodes that intrinsically eliminate electrode deterioration during cycling. To scale up the dual-plating battery, we fabricated large cells and obtained capacities up to 10.8 A h at a cell volume of 3176 cm^3 (electrolyte volume is 1443 cm^3) (Fig. 4(e) and Fig. S19, ESI†). This capacity outperforms most previously reported aqueous batteries that rely on ion intercalation or deposition/dissolution mechanisms (Fig. 4(f)).[6,26–34] In our dual-plating system, the capacity is influenced by the ion concentration, volume of the electrolyte, and the energy efficiency. To scale up the capacity under a constant ion concentration, it is also necessary to improve the energy efficiency by, for example, exploring catalysts to boost the I^-/I_2 redox reaction kinetics.

The capacity of our designed DPZIBs primarily derives from the carrier ions instead of number of ions intercalated into host lattices or involved in solid–liquid conversion reactions.

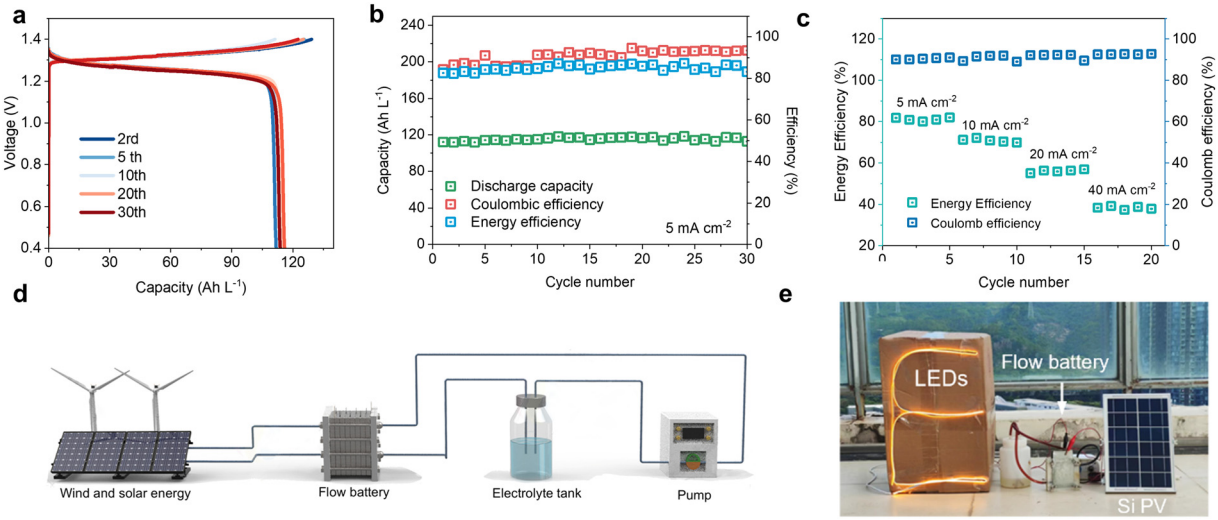

Fig. 5 Proof-of-concept membrane-free flow battery based on the DPZIB. (a) GCD curves, (b) cycling performance and (c) rate capability. (d) Schematic illustration of the integration of membrane-free DPZIB flow battery in grid-scale energy storage system, and (e) a prototype that continuously powers a LED light chain (5 W).

This allows an independent engineering of power and energy in a flow battery by adjusting electrolyte conditions and electrode surface area. As a proof of concept, we assembled a flow Zn–I_2 battery without using an ion exchange membrane to separate the catholytes and anolytes (Fig. S20, ESI†). This membrane-free configuration renders rapid charge transfer and lowers the manufacturing cost, making it suitable for scalable energy storage. In this setup, a relatively high concentration of iodine ions (4 M) was utilized to enhance the energy density. At a constant charging capacity of 2.65 A h at the current of 10 mA cm^{-2}, no significant capacity decay or energy efficiency drop was observed over 30 cycles (Fig. 5(a) and (b)). This suggests minimal side reactions during cycling. Moreover, the coulombic efficiencies under a flow mode at a wide range of currents (5–40 mA cm^{-2}) are relatively stable, although the values are all lower than 100% in the large-sized cells (Fig. 5(c)). The low efficiencies could be related to the temperature fluctuations from day to night and variations at the flow reaction interfaces. Furthermore, these Zn–I_2 flow battery modules can be integrated with green energy harvesting devices to buffer the intermittent nature of solar and wind energy, offering a continuous power supply to household electronics such as LED light chains from the day to the night (Fig. 5(d) and (e)). Considering the high cycling stability, intrinsic safety, and low cost of the membrane-free DPZIBs, we envision its potential as a safe alternative to Li-ion batteries in grid-scale energy storage. The next step is to further improve the working voltage and rate performance.

Conclusions

We have demonstrated a low-cost, highly reversible dual-plating Zn–I_2 battery *via* the redox-active ZnI_xG4 complexes in an aqueous electrolyte. This system differs from the conventional $I^- \leftrightarrow I_2$ reactions of the iodine cathode by eliminating the active cathode materials or complex electrode frameworks. Hence, it simplifies the manufacturing process for active materials and electrodes, an essential step in traditional metal-ion batteries. The energy storage is realized based on the principles of the synergistic halogen-complexation chemistry, where G4 serves as an electron donor to increase the interaction between Zn and I. Meanwhile, the reconstructed Zn^{2+} solvated structure corresponds to the reduction of free iodine and improvement in the conversion efficiency. Moreover, this designed reaction redox also bypasses the challenges of polyiodide shuttling, self-discharge and zinc corrosion, all being crucial to the implementation of aqueous batteries for large-scale application. A prototype energy harvesting system is demonstrated by integrating the DPZIB, Si photovoltaics, and LEDs.

Nonetheless, the present challenges for its application in grid-scale energy storage include the relatively low energy density and rate performance compared to the mainstream lithium ion batteries and vanadium redox flow batteries. Possible approaches include anode-free configuration, further optimization of electrolytes, and exploration of catalysts.

Data availability

The data supporting this article have been included as part of the ESI.†

Conflicts of interest

The authors declare no competing financial interest.

Acknowledgements

The authors appreciate the financial support from the National Research Foundation, Singapore, under its Singapore–China Joint Flagship Project (Clean Energy) and the Singapore

Ministry of Education, under its AcRF Tier 1 project (RT8/22), the Joint Funds of the National Key Research and Development Program of China (2019YFA0705703), Guangdong Innovative and Entrepreneurial Research Team Program (2021ZT09L197), Guangdong Basic and Applied Basic Research Foundation (2023B1515120099). M. Y. Chuai thanks the financial support from the Postdoctoral Fellowship Program (GZC20232668).

Notes and references

1 J. Meng, Q. Tang, L. Zhou, C. Zhao, M. Chen, Y. Shen, J. Zhou, G. Feng, Y. Shen and Y. Huang, *Joule*, 2020, **4**, 953.
2 Z. Zhu, T. Jiang, M. Ali, Y. Meng, Y. Jin, Y. Cui and W. Chen, *Chem. Rev.*, 2022, **122**, 16610.
3 G. Choi, P. Sullivan, X. L. Lv, W. Li, K. Lee, H. Kong, S. Gessler, J. R. Schmidt and D. Feng, *Nature*, 2024, **635**, 89.
4 W. Fan, H. Wang and J. Wu, *eScience*, 2024, **4**, 100248.
5 H. Li, M. Zhang, Z. Zheng, X. Wu, X. Xiao, Z. Piao, C. Li, Y. Jia, J. Yang and G. Zhou, *Adv. Mater.*, 2024, e2409771.
6 Z. Zheng, X. Zhong, Q. Zhang, M. Zhang, L. Dai, X. Xiao, J. Xu, M. Jiao, B. Wang, H. Li, Y. Jia, R. Mao and G. Zhou, *Nat. Commun.*, 2024, **15**, 753.
7 J. J. Hong, L. Zhu, C. Chen, L. Tang, H. Jiang, B. Jin, T. C. Gallagher, Q. Guo, C. Fang and X. Ji, *Angew. Chem., Int. Ed.*, 2019, **58**, 15910.
8 L. Yuan, J. Hao, B. Johannessen, C. Ye, F. Yang, C. Wu, S.-X. Dou, H.-K. Liu and S.-Z. Qiao, *eScience*, 2023, **3**, 100096.
9 D. E. Ciurduc, C. de la Cruz, N. Patil, A. Mavrandonakis and R. Marcilla, *Mater. Today Energy*, 2023, **36**, 101339.
10 K. Xu, X. Zheng, R. Luo, J. Sun, Y. Ma, N. Chen, M. Wang, L. Song, Q. Zhao and W. Chen, *Mater. Today Energy*, 2023, **34**, 101284.
11 P. F. Zhang, J. H. Li, S. J. Zhang, D. C. Li, S. Y. Zeng, S. L. Xu, Q. X. Yao, L. Y. Liu, L. Ding, H. X. Li, Y. Y. Hu, J. T. Li and Y. Zhou, *Adv. Funct. Mater.*, 2023, **34**, 2306359.
12 Q. Zhang, Y. Ma, Y. Lu, Y. Ni, L. Lin, Z. Hao, Z. Yan, Q. Zhao and J. Chen, *J. Am. Chem. Soc.*, 2022, **144**, 18435.
13 S. J. Zhang, J. Hao, H. Li, P. F. Zhang, Z. W. Yin, Y. Y. Li, B. Zhang, Z. Lin and S. Z. Qiao, *Adv. Mater.*, 2022, **34**, e2201716.
14 H. Zhao, D. Yin, Y. Qin, X. Cui, J. Feng, Y. Zhang, L. Zhao, N. Gao, M. Cui, C. Xiao, G. Feng, Y. Su, K. Xi and S. Ding, *J. Am. Chem. Soc.*, 2024, **146**, 6744.
15 W. Li, H. Xu, H. Zhang, F. Wei, T. Zhang, Y. Wu, L. Huang, J. Fu, C. Jing, J. Cheng and S. Liu, *Energy Environ. Sci.*, 2023, **16**, 4502.
16 B. Li, Z. Nie, M. Vijayakumar, G. Li, J. Liu, V. Sprenkle and W. Wang, *Nat. Commun.*, 2015, **6**, 6303.
17 Q. Zhang, Y. Ma, Y. Lu, X. Zhou, L. Lin, L. Li, Z. Yan, Q. Zhao, K. Zhang and J. Chen, *Angew. Chem., Int. Ed.*, 2021, **60**, 23357.
18 X. Zheng, Z. Liu, J. Sun, R. Luo, K. Xu, M. Si, J. Kang, Y. Yuan, S. Liu, T. Ahmad, T. Jiang, N. Chen, M. Wang, Y. Xu, M. Chuai, Z. Zhu, Q. Peng, Y. Meng, K. Zhang, W. Wang and W. Chen, *Nat. Commun.*, 2023, **14**, 76.
19 Y. Gao, M. Wang, H. Wang, X. Li, Y. Chu, Z. Tang, Y. Feng, J. Wang, Y. Pan, Z. Ma, Z. Yang, D. Zhou and X. Li, *J. Energy Chem.*, 2023, **84**, 62.
20 W. Li, L. Huang, H. Zhang, Y. Wu, F. Wei, T. Zhang, J. Fu, C. Jing, J. Cheng and S. Liu, *Matter*, 2023, **6**, 2312.
21 H. Yang, Y. Qiao, Z. Chang, H. Deng, P. He and H. Zhou, *Adv. Mater.*, 2020, **32**, e2004240.
22 H. Gan, H. Li, M. Xu, C. Han and H.-M. Cheng, *Joule*, 2024, **8**, 3054.
23 P. Hei, Y. Sai, W. Li, J. Meng, Y. Lin, X. Sun, J. Wang, Y. Song and X. X. Liu, *Angew. Chem., Int. Ed.*, 2024, **63**, e202410848.
24 F. Yang, J. Long, J. A. Yuwono, H. Fei, Y. Fan, P. Li, J. Zou, J. Hao, S. Liu, G. Liang, Y. Lyu, X. Zheng, S. Zhao, K. Davey and Z. Guo, *Energy Environ. Sci.*, 2023, **16**, 4630.
25 A. Zhou, H. Wang, X. Hu, F. Zhang, Y. Zhao, Z. Hu, Q. Zhang, Z. Song, Y. Huang, L. Li, F. Wu and R. Chen, *Sci. Bull.*, 2023, **68**, 2170.
26 N. Hu, W. Lv, W. Chen, H. Tang, X. Zhang, H. Qin, D. Huang, J. Zhu, Z. Chen, J. Xu and H. He, *Adv. Funct. Mater.*, 2023, **34**, 2311773.
27 J. Huang, Y. Zhong, H. Fu, Y. Zhao, S. Li, Y. Xie, H. Zhang, B. Lu, L. Chen, S. Liang and J. Zhou, *Adv. Mater.*, 2024, **36**, e2406257.
28 L. Ma, Y. Ying, S. Chen, Z. Chen, H. Li, H. Huang, L. Zhao and C. Zhi, *Adv. Energy Mater.*, 2022, **12**, 2201322.
29 S. S. Shinde, J. Y. Jung, N. K. Wagh, C. H. Lee, D.-H. Kim, S.-H. Kim, S. U. Lee and J.-H. Lee, *Nat. Energy*, 2021, **6**, 592.
30 Y. Wang, L. e Mo, X. Zhang, Y. Ren, T. Wei, Y. He, Y. Huang, H. Zhang, P. Tan, Z. Li, J. Zhou and L. Hu, *Adv. Energy Mater.*, 2024, **14**, 2402041.
31 W. Wu, C. Li, Z. Wang, H.-Y. Shi, Y. Song, X.-X. Liu and X. Sun, *Chem. Eng. J.*, 2022, **428**, 131283.
32 Y. Xu, M. Zhang, R. Tang, S. Li, C. Sun, Z. Lv, W. Yang, Z. Wen, C. C. Li, X. Li and Y. Yang, *Energy Environ. Sci.*, 2024, **17**, 6656.
33 L. Hu, C. Dai, Y. Zhu, X. Hou, Z. Liu, X. Geng, H. Wang, J. Chen, N. Sun, Q. Rong, Y. Zhu, X. He and Y. Lin, *Energy Environ. Sci.*, 2024, **17**, 5552.
34 Z. He, J. Guo, F. Xiong, S. Tan, Y. Yang, R. Cao, G. Thompson, Q. An, M. De Volder and L. Mai, *Energy Environ. Sci.*, 2023, **16**, 5832.

